Available online at www.sciencedirect.com
ScienceDirect
Earth and Planetary Science Letters 249 (2006) 14–28
EPSL
www.elsevier.com/locate/epsl

New insights into the development of brittle shear fractures from a 3-D numerical model of microcrack interaction

David Healy [a,*], Richard R. Jones [b], Robert E. Holdsworth [a]

[a] *Reactivation Research Group, Department of Earth Sciences, University of Durham, Durham DH1 3LE, United Kingdom*
[b] *e-Science Research Institute, University of Durham, Durham DH1 3LE, United Kingdom*

Received 8 August 2005; received in revised form 1 June 2006; accepted 5 June 2006
Available online 8 August 2006
Editor: Scott King

Abstract

Existing models of brittle shear failure are unable to account for three-dimensional deformation involving the development of polymodal sets of fractures. Motivated by field observations of contemporaneous arrays of quadrimodal faults and deformation bands, we use an idealised micromechanical model to explain how brittle shear fractures can form oblique to all three remote principal stresses. We model tensile microcracks as finite ellipsoidal voids, subjected to small opening strains, in a linear isotropic elastic matrix. The geometry of the tensile stress lobes around the ends of an isolated microcrack promotes the *en echelon* interaction of neighbouring cracks with respect to the prescribed crack orientation. Coalescence of these interacting crack arrays into a through-going composite fracture surface leads to a brittle shear failure plane oriented obliquely to all three coordinate axes and all three remote principal stresses. Experimental evidence supports the idea that composite shear fractures can propagate in-plane through the coalescence of many constituent tensile microcracks. Our new model, based on the 3-D geometry of the elastic stress field around a mode I crack, can explain the oblique orientations of polymodal faults formed in a triaxially compressive stress field.

Keywords: Microcrack; Interaction; Fracture; Fault; Polymodal; Quadrimodal

1. Introduction

Existing theory for brittle shear failure in rocks fails to explain the deformation in three-dimensions. Consequently, our understanding of rock failure, derived from Coulomb's seminal 18th century study [1], is unable to account for a frequently observed class of natural fractures, in which quadrimodal fault sets display orthorhombic symmetry [2–6]. The Andersonian model of faulting [7], based on the Coulomb–Mohr failure criterion (e.g. [8]), can explain conjugate (i.e. bimodal) sets of normal, wrench or thrust faults, but conjugate faulting produces two-dimensional (2-D) plane strains (Fig. 1a). Polymodal fault arrays including quadrimodal fault sets (Fig. 1b), are able to accommodate the three-dimensional (3-D) strains that must inevitably arise from deformation caused by oblique lithospheric plate motion (e.g. [9,10]).

A model describing the strain due to slip along *pre-existing* quadrimodal faults has been presented by Reches [2,3]. However, to date there is no accepted model of fracture initiation and growth that can explain the distinct geometrical arrangement of *newly formed*

* Corresponding author. Fax: +44 191 334 2301.
E-mail address: david.healy@durham.ac.uk (D. Healy).

0012-821X/$ - see front matter © 2006 Elsevier B.V. All rights reserved.
doi:10.1016/j.epsl.2006.06.041

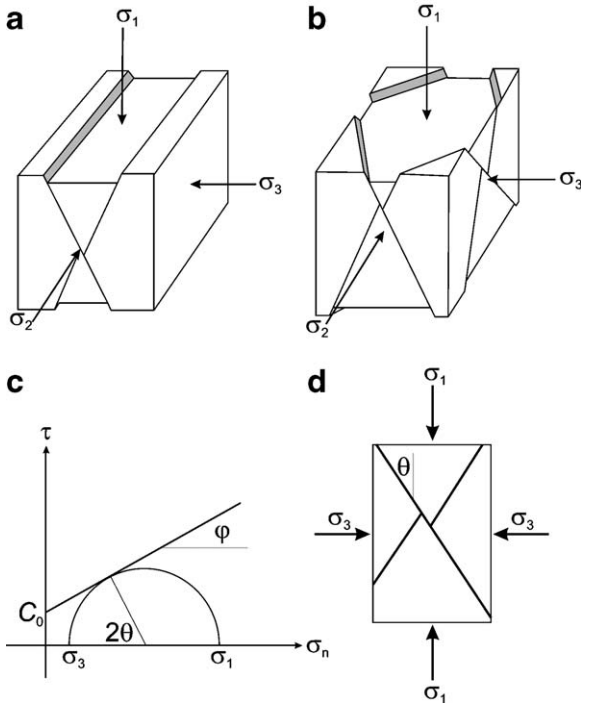

Fig. 1. Contrasting patterns of conjugate (bimodal) and polymodal faults. a) Conjugate faults form symmetrically about the remote σ_1 direction, which bisects the acute angle between the planes, and intersect along a line parallel to the remote σ_2 direction. b) Quadrimodal faults intersect to form rhombohedral traces on outcrop surfaces with σ_1 and σ_2 bisecting the acute angles between the failure planes. c) Mohr circle for bimodal faulting showing the relationship between the principal stresses at failure, the cohesive strength C_0 and the failure angle θ. d) Conjugate brittle shear failure planes inclined at acute angle θ to the maximum compressive stress σ_1.

quadrimodal fault planes. In this paper, we present a new model for rock failure based on the interaction of tensile cracks in 3-D to explain the observed angular relationships between quadrimodal shear failure planes and the principal remote stresses.

The overall purpose of this study is twofold: firstly, in comparison to the existing 2-D models of fracture development, a 3-D model will improve our theoretical understanding of brittle deformation processes. Secondly, since fault planes can act as either conduits or barriers to fluid flow, the precise geometry, and hence connectivity of fault networks or 'meshes' [11], can have a significant impact on fluid flow through fractured reservoirs (e.g. [12]). The model we present here can be applied to predict the geometric patterns of naturally developed fractures formed due to 3-D strain in sub-surface environments.

In this study, we focus on the geometry of newly formed brittle shear failure planes in 3-D. We first review existing models for brittle shear failure in rocks, with particular emphasis on model predictions for the orientation of failure surfaces. We then present our own field observations from an array of contemporaneous non-conjugate faults from outcrops in the UK, before developing a new model for the formation of shear fractures through the interaction and coalescence of mode I microcracks in 3-D.

2. Existing models of brittle shear failure

2.1. Macroscopic failure criteria

At the macroscopic level, the Coulomb–Mohr failure criterion [8] adequately predicts the orientation of conjugate bimodal fault planes under plane strain conditions. In the brittle regime, shear failure planes are predicted to form along either of two planes inclined at acute angles $\pm\theta$ to the direction of the maximum compressive stress σ_1 (see Fig. 1c–d) and which lie parallel to (i.e. contain) the direction of the intermediate stress σ_2. The relationship between the shear stress τ along the shear plane and the normal stress σ_n across it is given by

$$\tau = C_0 + \mu \cdot \sigma_n \tag{1}$$

where μ is the coefficient of internal friction and C_0 is the cohesive strength of the rock. The angle of failure θ can be expressed in terms of the angle of (internal) friction ϕ as

$$\theta = \pi/4 - \phi/2 \tag{2}$$

For brittle rocks deformed in the Earth's crust with a coefficient of internal friction taken as 0.6 [13], θ works out at c. ±31°, consistent with many field and laboratory observations. Eq. (1), which marks the onset of shear failure, can be recast in terms of the principal stresses acting on the rock as

$$\sigma_1[(\mu^2+1)^{1/2} - \mu] - \sigma_3[(\mu^2+1)^{1/2} + \mu] = 2C_0 \tag{3}$$

We suggest that the expression of the widely used Coulomb–Mohr criterion in terms of a single failure angle (θ), together with the absence of σ_2 from the failure equation (Eq. (3)) acts to conceal any role for the third spatial dimension during brittle shear failure of rocks.

The role of σ_2 in brittle shear failure has long been the subject of debate, (e.g. [14]). The stress state at depth within the lithosphere is likely to be triaxially compressive and the orientation of shear fractures formed under these conditions might be expected to be influenced by all three principal stresses. Motivated by the clay-cake experiments of Oertel [15], Reches employed field observations [2] and polyaxial (i.e. truly triaxial) rock deformation experiments [16] to investigate the strains produced by

slip along pre-existing polymodal faults [2,3]. He arrived at an empirical *slip* criterion (note: not a *failure* criterion), involving the first and second invariants of the principal stress tensor, and two constants estimated by curve fitting for different rock types.

Many other brittle failure criteria have been proposed in the past (for a recent review see [17]). However, few of these other criteria are able to predict the orientations of the shear failure plane which differ significantly from those of the Coulomb–Mohr criterion, i.e. two conjugate shear planes inclined at an acute angle to σ_1, and parallel to σ_2.

2.2. Experimental work on brittle shear failure in rocks

Rock deformation experiments in the laboratory have provided much useful data on the nature and orientation of brittle shear fractures (for a review see [18]). Note that most so-called 'triaxial' experiments conducted in the compressive regime are in fact uniaxial, with an axially applied load (σ_1) greater than a radial load ($\sigma_2=\sigma_3$) applied through a confining jacket. Many experiments confirm the general form of the Coulomb–Mohr criterion, both in terms of the magnitude of the applied stresses at failure and the angle of failure with respect to σ_1. An important finding is that, in detail, the shear fracture surface is often not smooth, with a trace that follows a 'staircase' trajectory, e.g. see Fig. 14 of Moore and Lockner [19]. The angle of shear fracture relative to σ_2 or σ_3 is rarely measured, but we anticipate that it is also not smooth (for a rare published example see [20], their Fig. 16). This inherent roughness of newly formed shear fractures is consistent with their composite nature and supports micromechanical models of shear fracture growth through crack interaction and coalescence (see below).

Reches and Dieterich [16] carried out polyaxial rock deformation experiments by varying the applied strain rates on the sample. This enabled them to *measure* the orientation of the final shear failure surface with respect to the applied strains and, by inference, the applied stresses. Using cubic samples of granite, sandstone and limestone deformed under controlled strain rates, and taking care to eliminate shear stresses at the piston-sample interface, Reches and Dieterich generated multimodal shear fractures oriented at varying degrees of obliquity to the applied stresses ([16], their Figs. 2 and 3). Oertel [15] also produced multimodal fault patterns in analogue experiments with clay, although the rheology of this material makes it difficult to extend his analysis to brittle rocks.

Experimental results have lead to the widespread acceptance that brittle shear fractures nucleate and propagate through the interaction and eventual coalescence of tensile microcracks. Microstructural observations of deformed samples (e.g. [21,22,19]) and the recording of acoustic emission (AE) data during rock deformation experiments [23,24] suggest that the localisation of tensile microcrack arrays occurs in the region of the final shear fracture. The coalescence of the interacting microcracks into a through-going shear fracture is catastrophic and occurs just prior to sample failure (e.g. [25]). The prevailing view is that the majority of these tensile microcracks are oriented parallel to the σ_1–σ_2 plane in the sample, for example see Fig. 3 of Peng and Johnson [21] and Fig. 14 of Reches and Lockner [26]. The cumulative effect of many microcracks with mode I opening leads to the onset of positive dilatancy before failure.

2.3. Micromechanical models of shear failure

Physical explanations of brittle shear failure have been developed using a variety of micromechanical models. Building on the concept of Griffith cracks [27,28] in an elastic solid, Brace [29] and Brace and Bombolakis [30] suggested that pre-existing microcracks inclined to a compressive σ_1 would deform in mode II (shear). Fracture mechanics theory suggests that shear cracks cannot propagate in their own plane. Using photoelastic plastic and glass, Brace and Bombolakis [30] showed that tensile 'wing' cracks develop at the tips of shear cracks. These 'wing' cracks propagate in a curved path, towards the applied σ_1 direction. Their model suggests that arrays of interacting shear and tensile 'wing' cracks could coalesce to form a through-going shear fracture (see Fig. 2a and [30], their Fig. 4). Horii and Nemat-Nasser [31] presented a detailed quantitative basis for this model. However, microstructural observations from experimentally deformed rocks by Peng and Johnson [21] suggest that the majority of microcracks were tensile and grew parallel to σ_1–σ_2, a finding supported more recently by Reches and Lockner [26].

Reches and Lockner [26] based their model for shear fracture development on the interaction of tensile microcracks aligned parallel to the plane of σ_1–σ_2 (Fig. 2a). Using a standard solution for the elastic field around a mode I crack from Pollard and Segall [32], Reches and Lockner [26] calculated the locus of maximum tensile interaction for a given microcrack and found it to be inclined at an acute angle to σ_1, typically in the range of 20–30°. This angle exerts a fundamental control on the geometry of the final shear failure plane by promoting *en echelon* interaction of neighbouring cracks. The tensile

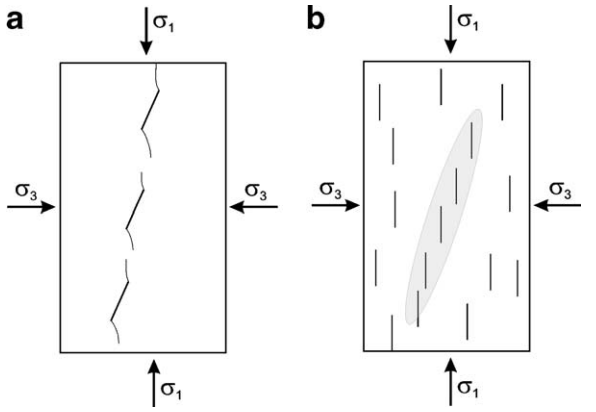

Fig. 2. Differing concepts of crack interaction. a) Tensile mode I crack interaction, after [26]. Microcracks initially form and dilate throughout the rock mass, but interactions among *en echelon* cracks generate a shear plane nucleus (grey shade) inclined at approximately 30° to the maximum compressive stress σ_1. b) Shear and 'wing' crack interaction, after [30]. Pre-existing optimally oriented Griffith cracks activate in mode II shear. Tensile mode I 'wing' cracks form at the tips of the shear cracks, initially at a high angle but growing towards the direction of the maximum compressive stress σ_1. Through-going shear failure results from coalescence of shear and 'wing' cracks arranged *en echelon*.

stress field of a crack acts to open neighbouring cracks in zones above and below and to either side of itself; cracks located alongside fall in the compressive field and tend to be closed. The combined field from two interacting *en echelon* cracks extends over a wider area than those of individual cracks, leading to a self-organising runaway of the shear fracture nucleus. The Reches and Lockner model successfully explains the final geometry of brittle shear failure planes and is consistent with the bulk of experimental evidence for pre-failure localised tensile microcracking. However, in their model, the core concept taken from Pollard and Segall [32] is that of a mode I tensile crack *infinite* in the direction parallel to σ_2 (the z coordinate axis of Reches and Lockner [26]; the x_3 axis of Pollard and Segall [32]). The interaction and eventual coalescence of these 'blade-like' or tabular cracks cannot predict a shear failure plane oblique to σ_2, and therefore cannot explain polymodal faulting in non-plane strain conditions.

The detailed mechanisms of the actual coalescence among arrays of interacting microcracks have been described by Sammis and Ashby [33] and King and Sammis [34] in terms of buckling 'beams' of intact rock between arrays of opening cracks. However, the dominant control on the orientation of the final through-going fracture is from the earlier interaction of microcracks, rather than their eventual coalescence [23,26]. The mechanisms of coalescence may slightly alter the orientation of the final shear fracture, but we do not consider the details of microcrack coalescence further in this study.

3. Field observations of quadrimodal faults

There are many documented cases of fractured rocks containing polymodal fracture sets. Reches [2] reviewed field examples of quadrimodal faults. Aydin and Reches [4] provided detailed measurements from the Chimney Rock area in Utah (USA), although the contemporaneity of the four constituent fracture sets in this area has recently been questioned by Davatzes et al. [35]. Krantz [5,6] developed the odd-axis technique to estimate the 3-D strain field from measurements of orthorhombic fault sets. Koestler and Ehrmann [36] measured a quadrimodal fault array in the Chalk of northern Germany. Jones and Tanner [37] and Jones et al. [38] documented polymodal fracture sets across a large area of central Scotland. More recently, Crider [39] has modelled elastic interactions among an array of normal faults in Oregon (USA) which display a clear quadrimodal pattern at the map (km) scale (see Fig. 3 of [39]). Imber et al. [40] have recorded large-scale quadrimodal faulting in 3-D seismic data on the Norwegian Atlantic margin. De Paola et al. [41] described small-scale quadrimodal faults in sandstones around the 90 Fathom Fault in NE England. Here we present additional field observations of demonstrably contemporaneous polymodal non-conjugate fault sets from the UK.

3.1. Gruinard Bay, NW Scotland

At Gruinard Bay in Wester Ross (Fig. 3a–b), Triassic sandstones and conglomerates were deformed during the Mesozoic development of the Minch Basin. Extensional brittle strain is recorded within these rocks from km-scale normal faults down to arrays of discrete deformation bands, each with up to a few millimetres of normal offset. These deformation bands display shear offsets of laminations in the sandstone and represent brittle shear fractures. Bedding in the sandstones remains sub-horizontal and many exposed bedding planes reveal the traces of four distinct sets of deformation bands (see Fig. 3c). Note that in 2-D cross-sections normal to bedding (Fig. 3d), these faults display apparently conjugate geometries. Measurements of deformation band orientation taken from small (<5 m^2) domains of contiguous outcrop reveal clear polymodal or quadrimodal patterns when plotted as poles on a stereonet (see Fig. 3e).

For the domain with the largest number of measurements ($n=75$), we group the orientation data into four sets based on fracture strike and dip direction: 030/WNW, 030/ESE, 060/NW and 060/SE. As discussed by Potts and

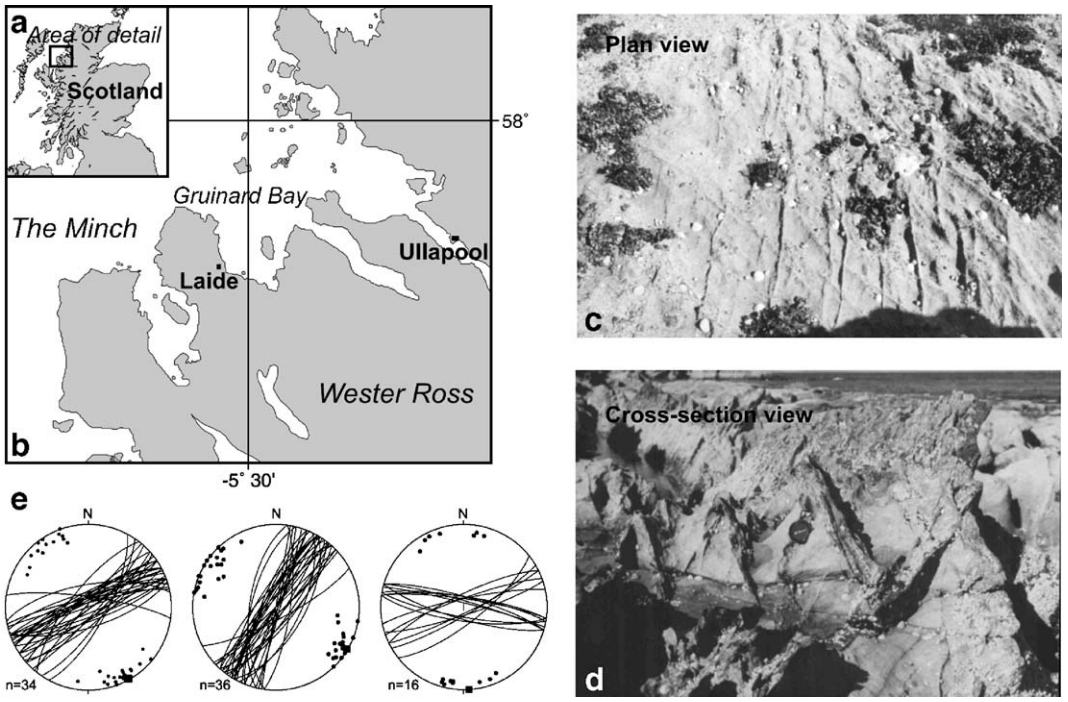

Fig. 3. Field data from Gruinard Bay, NW Scotland. a) Map of Scotland with Gruinard Bay enclosed by rectangle. b) Map of Gruinard Bay. c) Photograph of a bedding surface in Triassic sandstones on the foreshore North of Laide. Fracture traces occur as distinct ridges in four sets of deformation bands. d) Photograph showing a cross-section at a high angle to bedding, with *apparent* conjugate traces of deformation bands from the four distinct sets. e) Lower hemisphere equal area stereonets of poles to deformation bands measured at three stations North of Laide. Each station covers <5 m^2 of contiguous outcrop.

Reddy [42,43], the number of different possible deformation histories, h_c, that can account for a given number, n, of separate fracture sets is given by:

$$h_c = (n-1)! \tag{4}$$

such that for four fracture sets, $h_c = 3! = 6$. The number of different cross-cutting relationships, p_c, that need to be established to determine the complete history for the fracture sets is:

$$p_c = n(n-1) \tag{5}$$

so that for four fracture sets we need to collect evidence from twelve different cross-cutting relationships to fully constrain the relative timing history. A systematic collection of shear offset relationships yielded the results shown as field sketches in Fig. 4 and from these data we have constructed a matrix of age relationships. These data demonstrate that members of each fracture set were active (i.e. accumulating shear offset), contemporaneously with each of the other sets. In common with other faulted high-porosity sandstones elsewhere (e.g. [44,4,45]), slip along shear planes involving cataclasis leads to strain-hardening behaviour and therefore rules out subsequent reactivation in another stress field as an explanation for the mutual shear offsets. Furthermore, microstructural measurements from deformation bands produced in the laboratory reveal concentrations of microcracks aligned parallel to σ_1 consistent with their formation through the interaction and coalescence of tensile cracks [46]. In summary, the deformation bands observed at Gruinard Bay are brittle shear fractures displaying clear polymodal and quadrimodal patterns which formed synchronously.

4. Recent 2-D studies of fracture interaction

Several authors have studied interactions among various types of fractures, often with some form of simplifying 2-D approximation. The elastic interaction of arrays of tensile microcracks arranged *en echelon* have been studied by Du and Aydin [47], but their analysis was limited to plane strain. Lockner and Madden [48,49] modelled interactions among periodic arrays of cracks oriented either parallel, normal or at 45° to the maximum remote compressive stress in 2-D. Pollard et al. [50] also analysed *en echelon* arrays of

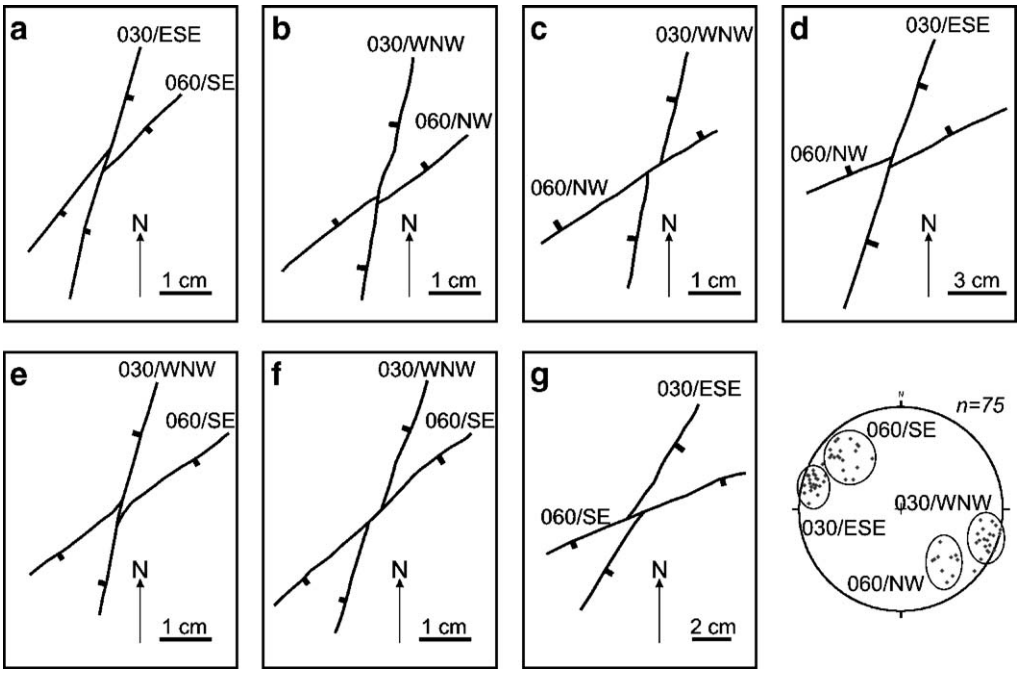

Fig. 4. Maps of deformation band shear offsets. A systematic search was conducted at the station with the largest number of data ($n=75$) for age relationships among the four sets of deformation bands. The clusters of poles on the stereonet were binned into four orientations based on approximate strike and dip direction. a–g show examples of mm-scale shear offsets among seven combinations of deformation bands (see Table 1). Note that the 060/NW deformation band in c is the same as that in d, viewed further along strike.

cracks emanating from the edge of a parent dilatant crack, with the modelled tensile cracks infinite in one dimension. At a larger scale, Crider and Pollard [51] studied the elastic interaction of an *en echelon* pair of dipping normal faults to explain the formation of breaching fractures in the relay zone. Crack interaction is the subject of intensive study in the field of materials science, particularly in relation to metal-matrix composites (MMC), where the focus is on calculating stress intensity factors for randomly oriented cracks, or estimating the effective elastic properties of a given material (e.g. see [52–54]).

Table 1
Matrix of age relationships for the deformation bands seen at Gruinard Bay

		Younger			
		030/ESE	030/WNW	060/NW	060/SE
Older	030/ESE		(not seen)	(not seen)	↙g
	030/WNW	↙c+d		↙c	↙f
	060/NW	↙d	↙b		(not seen)
	060/SE	↙a	↙e	(not seen)	

Each cell in the matrix represents a possible relative age determination among each of the four sets of fractures (see stereonet in Fig. 4). For these quadrimodal deformation bands, relative ages have been determined from observations of shear offset of one set (older) by another (younger). The lowercase letters in each cell refer to the field sketches in Fig. 4. Most of the 12 possible mutual relationships have been observed, and we infer that all four sets of fractures were contemporaneous.

5. Numerical modelling

The numerical model we present here is a micromechanical analysis of the development of fractures by the interaction and coalescence of individual microcracks, and is a further development of the analysis of Reches and Lockner [26]. In contrast to their model of tensile mode I cracks extending to infinity in one dimension, we model each tensile microcrack as a finite 3-D ellipsoidal void. We retain the simplifying concept of a homogeneous, isotropic linear elastic matrix, and focus on the *geometry* of the problem, i.e. to determine the 3-D distribution of elastic stress around interacting cracks and thereby explain the formation of shear fractures oblique to all principal stresses, as seen in quadrimodal fault patterns. Our model prescribes the location and geometry of these cracks, and the elastostatic nature of the solution does not incorporate tensile crack nucleation or propagation.

5.1. Eshelby's solution

To calculate the elastic stress field around an ellipsoidal void in 3-D we employ the solution of Eshelby [55,56]. Murrell and Digby [57] used Eshelby's solution to model Griffith cracks as 3-D voids in an elastic matrix. However, they restricted their analysis to non-interacting fields in order to find the optimum orientation for in-plane propagation of each Griffith crack.

Eshelby [55,56] derived the elastic field for two related problems, without recourse to ellipsoidal coordinates (e.g. [58]). The first solution is for the case of an inclusion with a prescribed strain enclosed within a matrix where the elastic properties of inclusion and matrix are the same. The prescribed inclusion strain, or 'stress-free transformation strain' of Eshelby [55], has been called the 'eigenstrain' by Mura [59]. Eigenstrains are non-elastic strains due to thermal expansion, phase transformation or twinning. Eshelby [55] produced the surprising result that if the inclusion is bounded by an ellipsoid, the total strain within the inclusion (the eigenstrain plus the strain due to constraint from the surrounding matrix) is uniform. This first result is then used to obtain a second more useful result for inclusions with material properties differing from those of the matrix. Eshelby [55] called these 'inhomogeneities' to distinguish them from 'inclusions' *sensu stricto*. Note that if the elastic properties of the inhomogeneity are set to zero, it becomes a void in an elastic matrix. Eshelby [55] calculated the elastic field due to an inhomogeneity with his 'equivalent inclusion' method. The equivalent inclusion has material properties identical to those of the matrix, but is subjected to an eigenstrain that produces the same total elastic field as the original inhomogeneity. Using the previous solution for the homogeneous inclusion an expression can be derived for the total field due to the inhomogeneity in terms of the known strains and material properties (see Chapter 4 of Mura [59] for a complete analysis).

Expressions for the external elastic field of spheroidal inclusions (prolate, oblate and spherical) have been presented in closed form by Ju and Sun [60,52]. In contrast to the elastic stress within the inclusion, the elastic stress (σ) outside an ellipsoidal inclusion varies with coordinate position (x), and can be expressed as

$$\sigma(x) = [\mathbf{C}^0 \cdot \mathbf{G}(x)] : \varepsilon^{*0} \tag{6}$$

where the symbol ":" denotes tensor contraction and $\mathbf{C}^0$ is the linear fourth order stiffness tensor of the elastic matrix. $\mathbf{G}$ is the Eshelby tensor for the external field, also a fourth order tensor and is similar in form to the $\mathbf{S}$ tensor for the interior field, but is position dependent. ε^{*0} is the eigenstrain within the inclusion. The value for ε^{*0} is calculated from

$$\varepsilon^{*0} = -[\mathbf{A} + \mathbf{S}]^{-1} : \varepsilon^0 \tag{7}$$

where $\mathbf{S}$ is the fourth order Eshelby tensor for the internal field, ε^0 is the prescribed strain within the inclusion and $\mathbf{A}$ is the fourth order elastic 'phase-mismatch' tensor of Ju and Sun [60,52]. This is given by

$$\mathbf{A} = [\mathbf{C}^1 - \mathbf{C}^0]^{-1} \cdot \mathbf{C}^0 \tag{8}$$

where $\mathbf{C}^1$ is the linear fourth order stiffness tensor of the inclusion.

To model a tensile microcrack as an ellipsoidal void, we set the elastic properties (stiffness tensor, $\mathbf{C}^1$) of the inclusion to zero. During brittle deformation of the lithosphere, dilatant tensile microcracks are likely to be filled with a hydrous fluid phase. At shallow depths (relatively low confining pressure), the elastic stiffness of this fluid will be very much reduced by comparison to the enclosing matrix, and we believe that setting the inclusion stiffness tensor to zero is a valid approximation. We only consider 'penny-shaped' cracks modelled as oblate spheroidal voids with semi-axes $a = b \gg c$. The length–width aspect ratio (a/c) of the modelled cracks is fixed at 100, with semi-axis c aligned parallel to our coordinate z direction (see Fig. 5a), to match the observations of preferred microcrack orientation in the σ_1–σ_2 plane (e.g. [21,26]). The elastic properties of the isotropic matrix are defined using a Young's modulus of 20 GPa and Poisson's ratio of 0.3, comparable with those of sandstone.

5.2. Elastic stress field of an isolated tensile crack in 3-D

The elastic stress field around an isolated tensile mode I crack is shown in Fig. 5, calculated from Eshelby's solution (after Ju and Sun [60,52]). The crack is modelled with an opening mode eigenstrain ε_{zz} of 2e–5, equivalent to a uniaxial tensile stress (or equivalent uniform internal pressure) of 1 MPa for the chosen elastic properties. Although we do not impose a remote compressive stress field in these models, we assume that tensile microcracks in a rock subjected to a triaxially compressive stress field will in general be aligned parallel to the remote σ_1–σ_2 principal plane, corresponding to our x–y coordinate plane.

Fig. 5c shows a contour plot of the σ_{zz} component of the stress tensor in the x–z plane. This normal stress component is the most important when considering

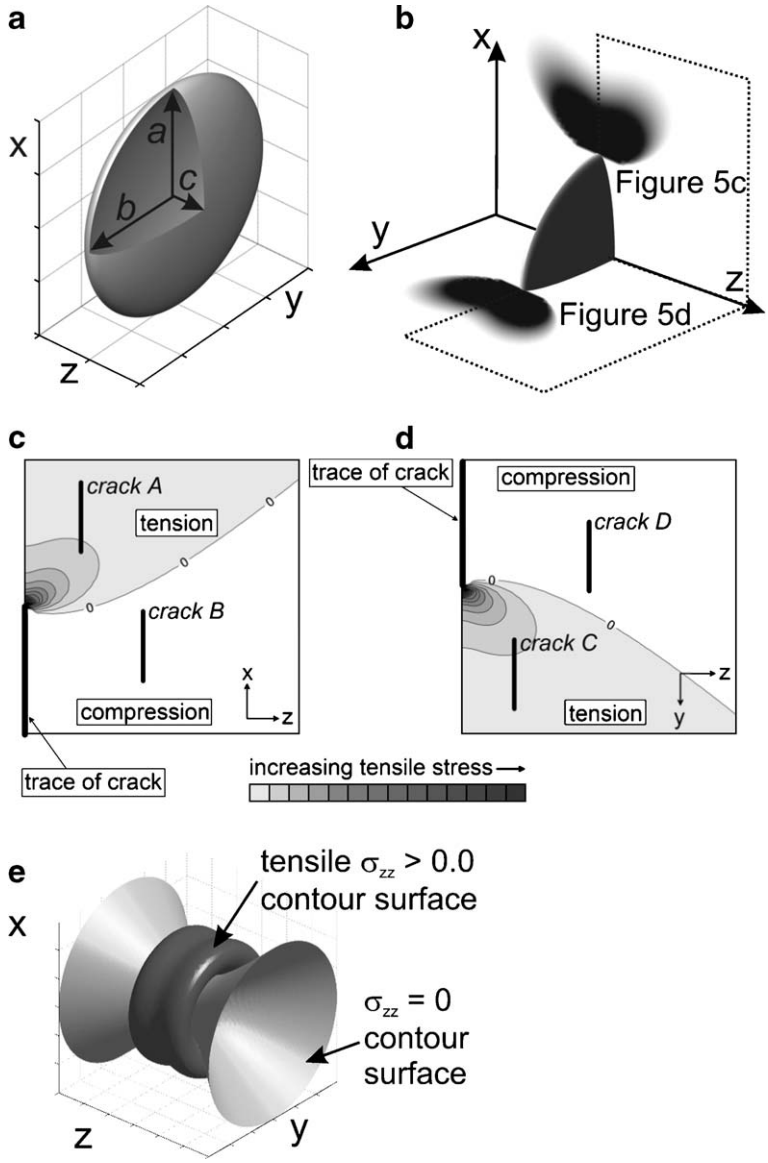

Fig. 5. Elastic stress field around an isolated 'penny-shaped' crack. a) Reference frame used in this study with a 'penny-shaped' tensile microcrack modelled as an oblate spheroidal void with semi-axes $a=b\gg c$, and aspect ratio (a/c) of 100. Semi-axes a, b and c are aligned with the x, y and z coordinate axes respectively. b) 3-D plot to show the elastic stress field around an isolated tensile crack. Mapped value is the σ_{zz} component of the perturbed stress field, which is the most important when considering tensile interactions of cracks oriented with their short c-axes parallel to z. Regions with compressive stress appear white; increasing tensile stress is shown as darker grey. c) Detail of the x–y region outlined in (b). Neighbouring crack A lies in the tensile field while crack B lies in the compressive field. Crack A will tend to be opened and crack B will tend to be closed by the elastic field of the parent crack. d) Detail of the y–z region outlined in (b). Neighbouring crack C lies in the tensile field of the parent crack, while crack D lies in the compressive field. Crack C will tend to be opened and crack D will tend to be closed by the elastic field of the parent crack. e) 3-D view of the isolated crack and the surrounding σ_{zz} field. The elastic stress field of an isolated crack will promote *en echelon* tensile interaction with neighbouring cracks in 3-D, and this interaction is not confined to a single (e.g. x–z) plane.

tensile interactions among mode I cracks. Compressive stress is not contoured and appears as white, while increased tensile stress is shown in a grey scale (higher tensile stress is darker). The form of the stress distribution is very similar to the results calculated by Reches and Lockner [26] (their Fig. 5) from the solutions of Pollard and Segall [32] for a mode I crack under uniaxial tension or uniform internal pressure, with bi-lobate regions of increased tensile stress at either end of the crack. A neighbouring tensile crack located in the tensile field of the modelled crack (e.g. crack A) will tend to be opened, while a crack in

the compressive region (e.g. crack B) will tend to be closed.

The location and shape of these lobes of increased tensile stress are well known from published 2-D solutions of elastic fields around mode I cracks. Eshelby's solution provides the complete 3-D elastic field around the ellipsoidal crack. Fig. 5d shows the σ_{zz} stress component in the y–z plane, orthogonal to that shown in Fig. 5c. For the 'penny-shaped' crack modelled here, symmetry predicts that the stress field in the y–z plane is identical to that in the x–z plane, and this is confirmed numerically using the Eshelby solution. This implies that stress interaction with neighbouring cracks also applies in this y–z plane, and indeed, throughout three-dimensional space. The *en echelon* character of this tensile stress interaction is seen to be a fundamentally 3-D feature of the model. In 3-D, the region of increased tensile stress around a tensile microcrack forms an indented ring-shaped, toroidal zone enclosing the crack and extending outwards from the crack tips (Fig. 5e).

For a given distance from the crack, the precise locus of the maximum tensile stress can be computed. This locus is derived from the value of the average crack normal stress (CNS) defined as

$$\mathrm{CNS}_{\mathrm{average}} = \int_{s-L/2}^{s+L/2} \sigma_{zz} \mathrm{d}s \qquad (9)$$

where L is the crack length (equal to $2a$, the ellipsoid semi-axis), and s is the crack parallel component of radial distance from the crack tip. We compute $\mathrm{CNS}_{\mathrm{average}}$ by numerical integration and then calculate the locus of the maximum of $\mathrm{CNS}_{\mathrm{average}}$ around the crack. This locus forms a hyperbola in 2-D (Fig. 6a) and this is the M curve of Reches and Lockner [26]. In 3-D it forms a one-sheeted hyperboloid (Fig. 6b) enclosing two conical tangential envelopes symmetrical about the z axis (Fig. 6c). These cones can be considered as the rotation of the tangents in Fig. 6a through 360° about the z axis. The angle θ these tangents make with any crack-parallel axis is a constant of the elastic stress field around an ellipsoidal crack, and for a narrow crack ($c \ll a$) is approximately ±26°. This is close to the value of ±34° reported by Reches and Lockner [26] from their 2-D model and we ascribe the discrepancy to the differences between 2-D and 3-D formulations of the stress field and a component of error from inexact numerical calculation. Shear fracture planes formed by tensile crack coalescence are equally likely to form in any orientation bounded by the outer surface of these cones (Fig. 6b). Irrespective of the spacing of the interacting cracks, the envelope to the locus of maximum tensile interaction provides a limiting angle controlling the relative position of cracks that are most likely to preferentially interact and coalesce. Assuming that shear fractures nucleate through the mutual interaction of

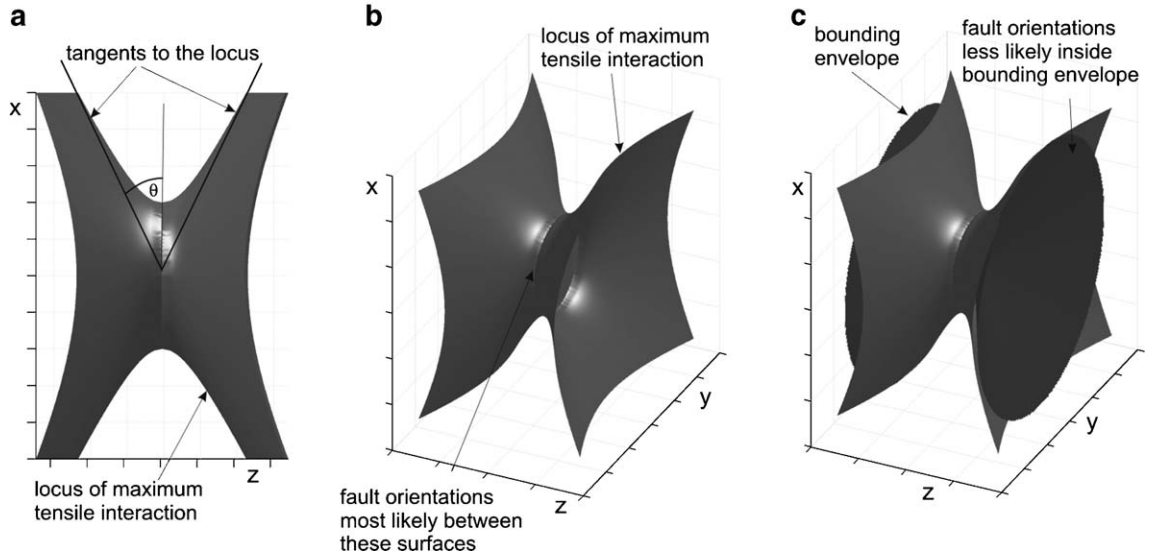

Fig. 6. Locus of maximum tensile interaction. a) side-on 2-D view of the locus of maximum tensile interaction The angle θ measures the inclination of the surface from the plane of the crack, and defines an upper limit to the orientation of likely shear fractures formed by interaction and coalescence among neighbouring cracks. Compare the edges of this surface to the M curve of Reches and Lockner [26] b) 3-D view of the locus of maximum tensile interaction, a hyperboloid with radial symmetry (for a 'penny-shaped' crack) about the z axis. c) 3-D view of the conical (light grey) tangential envelopes to the locus of maximum tensile interaction (dark grey). The most likely shear failure planes are expected to lie within the volume between the outer surfaces of the cones.

neighbouring tensile cracks, shear planes are therefore much less likely to develop at θ angles greater than 26°.

5.3. Interaction of ellipsoidal inclusions

The 3-D geometric form of the tensile stress around a single tensile microcrack has important implications for the stress interaction between neighbouring microcracks. Eshelby [60,52] derived his solution for the case of an isolated ellipsoid. Chalon and Montheillet [61] used Eshelby's solution to investigate the elastic interaction of spherical gas bubbles in an elastic matrix. In the case where the bubbles are of the same size and subject to the same pressure (i.e. the same eigenstrain), the total elastic strain field reduces to the linear superposition of the individual strain fields.

The distribution of tensile stress in 3-D around an isolated tensile mode I microcrack promotes interaction among *en echelon* arrays of mode I cracks. To explore the 3-D interaction of tensile microcracks, we calculate the total elastic stress fields for two arrays of three cracks each. The arrays are oriented so that they are coplanar with the principal axes of the far-field stress system. The crack spacing is 1 unit in z and 2.75 units in x or y. In all cases, the cracks are defined with semi-axes $a=b=1$ unit, $c=0.01$ unit.

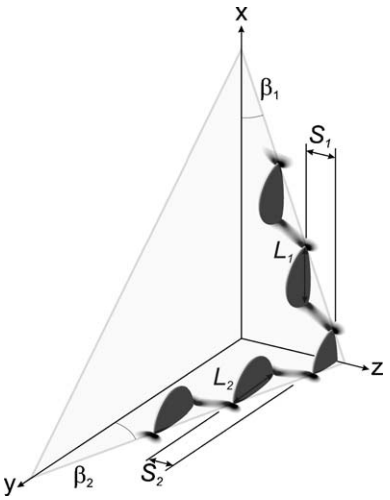

Fig. 7. Oblique 3-D view of a shear fracture formed through the interaction and coalescence of two orthogonal arrays of tensile cracks. Equidimensional penny-shaped cracks with their centres coplanar in the x–z and y–z coordinate planes. Increasing tensile σ_{zz} stress is shown as a grey shade, compressive stress is left white. Interaction of tensile stresses at the crack tips leads to increased tensile stress at each end of the whole array, when compared with an isolated crack, expanding the region of interaction. This self-organised expansion is believed to generate a run-away coalescence of the cracks and a through-going shear fracture [26]. The same pattern of interaction in the y–z plane to that in the x–z plane is clear. This implies that the interaction and eventual coalescence of arrays of tensile cracks arranged en echelon in 3-D will be oblique to the common flat plane of the tensile cracks, and oblique to all three coordinate axes and remote principal stresses.

The σ_{zz} component of the total elastic stress field for a 3-D *en echelon* array of six cracks is shown in Fig. 7. The lobes of increased tensile stress for each crack merge with those of the adjacent crack, and the stress at the ends of the array is increased relative to that of a single crack. This mutual amplification forms the basis for the self-organising nucleation and runaway propagation of the shear fracture nucleus [26]. For a given population of pre-existing tensile microcracks in a rock volume, these interactions will lead to the nucleation of a brittle shear failure plane inclined at an acute angle to the direction of remote σ_1 (our coordinate x), but also inclined to the direction of remote σ_2 (our coordinate y). Based on the geometry of tensile stress interaction calculated for the prescribed *en echelon* crack array, one possible orientation for a newly formed shear plane is shown (light shade in Fig. 7). The trace of this oblique shear plane makes an acute angle with the x axis (inferred direction of remote σ_1) in the x–z plane (remote σ_1–σ_3 plane), and within this plane conforms to existing macroscopic models of 2-D brittle shear failure (e.g. Coulomb–Mohr). However, the trace of the shear plane also makes an acute angle with the y axis (inferred direction of remote σ_2) in the y–z plane. The implication of these results, based on fundamental properties of the elastic field around tensile microcracks, is that 3-D crack interaction is likely to cause preferential fracture development in orientations oblique to all three remote principal stresses.

5.4. Orientation of newly formed brittle shear fractures in 3-D

In our 3-D models, and the 2-D models of Reches and Lockner [26], the locus of maximum tensile stress around each crack exerts a major control on the tensile interaction among neighbouring microcracks. A key issue is to determine the factors that control this locus. The position and orientation of this locus is not dependent on the opening strain (or stress) across the crack, the length–width aspect ratio of the crack, or the elastic moduli of the matrix. The pattern is self-similar for a range of crack openings, length–width ratios and/or variations in elastic moduli, and only the magnitude of the tensile stress varies. Therefore, for oblate spheroidal cracks, the angle θ (see Fig. 6a) between the tangent to the locus of maximum tension and the x axis (direction of remote σ_1), is effectively a constant for a given material.

Reches and Lockner [26] expressed their angle of failure β (equivalent to the angle θ in the Coulomb–Mohr criterion, Eq. (2)) as a function of crack spacing S, crack length L and the angle of the locus of maximum tension θ. In our 3-D model, the shear failure plane will in general be oblique, and not perpendicular to the x–z (remote σ_1–σ_3) plane. We label the angle between the *trace* of the shear failure plane in x–z and the direction of remote σ_1 as β_1 (see Fig. 7). The spacing of cracks in the z direction of the x–z plane is labelled S_1 and the length of the crack in the x direction is L_1 (=2a). The angle between the failure plane and the direction of σ_2 in the y–z (remote σ_2–σ_3) plane is labelled β_2 (see Fig. 7), the spacing of cracks in the z direction of the y–z plane is labelled S_2 and the length of the crack in the y direction is L_2 (=2b). Following Reches and Lockner [26] we can write

$$\beta_1 = \tan^{-1}\{[2(S_1/L_1)\sin\theta]/[\sin\theta + 2(S_1/L_1)\cos\theta]\} \quad (10)$$

and from our 3-D model we can show

$$\beta_2 = \tan^{-1}\{[2(S_2/L_2)\sin\theta]/[\sin\theta + 2(S_2/L_2)\cos\theta]\} \quad (11)$$

where θ is the angle of the tangent to the locus of maximum tensile stress (see Fig. 6). As discussed above, given the self-similarity of the shape of the elastic stress fields around isolated cracks, the angle θ is effectively a constant (for a given material). Therefore, in a crack interaction model with prescribed tensile microcracks, to explain any variation in shear failure plane orientation, we need variations in other parameter values. For a given rock with an initial distribution of microcracks where S_1=S_2, i.e. microcracks evenly spaced in all directions, the critical factor governing the orientation of the shear plane is the crack length. If $L_2 \gg L_1$, the angle β_2 will be less than β_1, and as L_2 increases, the shear failure plane will change orientation towards parallelism with σ_2. Therefore, if the tensile microcracks propagate such that L_2 increases with respect to L_1 ($b \gg a$), our 3-D model predicts the formation of apparently conjugate shear fracture planes, each containing the σ_2 direction. Similarly, oblique (e.g. polymodal or quadrimodal) shear fractures result from the interaction and coalescence of cracks of approximately equal length, i.e. 'penny-shaped' cracks with L_2=L_1. Lastly, if the initial cracks propagate in both directions, leading to high values of both L_1 and L_2 for given values of S_1 and S_2, minimal interaction results in very low values of β_1 and β_2 and the formation of stepped *en echelon* joints.

In this elastostatic model with prescribed initial cracks, the rheology of the material, in the form of the elastic moduli, does not exert a direct control over the orientation of the shear failure plane in 3-D. From the equations describing the angles (β_1 and β_2) between the failure plane and the remote principal stresses, it is the spacing (S) and the dimensions of the interacting microcracks (L=2a) that control the orientation of the shear failure plane in 3-D.

5.5. Comparison of modelling results and field data

Interpretation of brittle shear fracture data measured at Gruinard Bay is shown in Fig. 8a–c. The conical bounding envelopes for predicted shear fracture orientation trace out small circles on a stereonet. The bounding cones delimit zones of likely fracture plane orientation, and show very close fit between model predictions and field data. In the laboratory results of Reches and Dieterich [[26], their Fig. 5], their fracture data are also limited by a bounding envelope of just over 25°.

The field data in Fig. 8c cluster into four groups that show a quadrimodal pattern with orthorhombic symmetry. This higher-order symmetry is not predicted by our

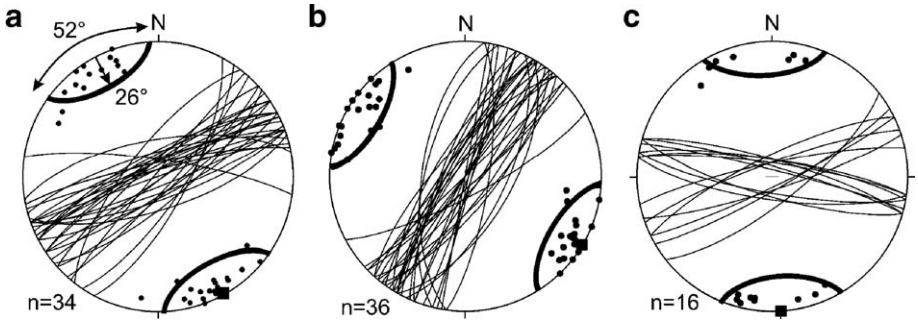

Fig. 8. Comparison of model predictions with field data. Faults measured in Triassic sandstones around Gruinard Bay, NW Scotland. All plots show lower-hemisphere equal-area stereonets with fracture planes plotted as poles and great circles. The square symbol marks the pole to the mean plane. The conical envelopes have been plotted as small circle girdles (bold) about the mean fracture direction, with apical angle 52° (2 × 26°) and a dip range of 90°–64° i.e. a maximum deviation from the vertical of 26°. The faults were measured at Laide waterfall (a), Laide jetty (b) and Udrigle (c).

model, but is explained by the slip model of Reches. Our future work will model the interactions of cracks of general ellipsoidal shape ($a>b>c$), rather than the spheroidal shapes ($a=b>c$) used in this study. We suspect that the orthorhombic symmetry of the stress field associated with true ellipsoidal cracks may impart significant changes to the 3-D form of the locus of maximum tensile interaction, as might the remote stress (strain) state or elastic anisotropy in the rock. These factors, absent in the current model, may promote the development of more ordered fracture sets such as quadrimodal arrays (Fig. 8c). We also note that natural and experimentally produced polymodal fault patterns often contain anastomosing and curvi-planar fracture surfaces. This variation in the orientation of macroscopic shear surfaces (Fig. 8a–b) may be controlled by mutually interacting microcracks preferentially located on the curvi-planar locus of maximum tensile interaction (Fig. 6b).

6. Discussion — limitations of the model

In our model we use arrays of equally spaced, equidimensional coplanar cracks in order to simplify the illustrations of stress interaction (Fig. 7), and to allow the derivation of simple, idealised expressions relating the geometry of the array to the final through-going shear plane (Eqs. (10) and (11)). In deforming rocks, the population of microcracks will be continually changing in response to the applied load. The dimensions of the microcracks and their spacing will evolve through time. Our elastostatic model with prescribed and fixed microcracks is effectively instantaneous and serves only to illustrate the general 3-D nature of the tensile stresses. We emphasize that the modelled stress patterns represent only the local perturbation to an overall stress field, created by the prescribed microcrack opening strain (stress), with no remote or other driving stress being applied. The addition of a non-hydrostatic stress to the models (e.g. by linear superposition), with $\sigma_1>\sigma_2>\sigma_3$, will create an asymmetry in the distribution of tensile stress around the z-axis. This asymmetry of the total stress field may help to explain the experimental observations of Reches and Dieterich [16], where the strain rate ratio, and therefore the stress ratio, correlates with changes in orientation of the quadrimodal fault planes.

Even allowing for these caveats, we prefer the fully 3-D solution of Eshelby to other quasi-3-D formulations, such as that for flat cracks published by Kassir and Sih [62]. These authors use a zero thickness, and therefore *zero volume,* elliptical crack geometry. Numerical models based on these quasi-3-D formulations cannot reproduce the ubiquitous positive dilatancy recorded in compressive shear failure experiments and do not permit different material properties to be prescribed within the inclusion.

In our elastostatic model, the prescribed microcracks do not propagate. This can be partially justified by considering rocks as heterogeneous polymineralic, polycrystalline aggregates in which individual mode I crack propagation is inhibited by the frequent juxtaposition of grains with differing material properties. This fundamental inhibition to mode I crack propagation may in fact tend to promote *interaction* at the expense of *propagation*.

Another key issue is how the nucleus of a new oblique shear fracture propagates into a through-going geological fault. Theory based on linear elastic fracture mechanics (LEFM), suggests that shear fractures cannot propagate in their own plane (for a review with geological applications see Petit and Barquins [63]). However, if natural shear fractures are composite and form through the interaction and coalescence of many tensile cracks, then the simplified geometry of a *single* shear crack used in LEFM models may be an invalid and irrelevant approximation. Propagation of a *composite* shear fracture may never be strictly in-plane to any of the constituent microcracks, but viewed at a larger macroscopic scale and allowing for surface roughness, the shear failure surface tends to propagate in-plane. This concept is supported by the acoustic emission (AE) data from rock deformation experiments when viewed in discrete time slices (e.g. [24], their Fig. 7). AE data viewed normal to the final shear fracture shows crescentic clouds of emissions (i.e. microcracking) surrounding the migrating edges of the shear plane nucleus. Viewed along the final shear fracture, emissions are confined to a linear band until the sample fails. Further experimental evidence for in-plane propagation of shear fractures is provided by the microstructural observations of Cox and Scholz [64,65]. Torsion experiments on granite produced a shear plane that propagated through obliquely oriented tensile cracks.

The matrix in our numerical models is an isotropic elastic material, and this is a limitation of the Eshelby [55,56] method. Fracture-induced anisotropy of rocks is well known (for a review see [66]), but there is increasing evidence that undeformed rocks also possess significant anisotropy in elastic properties (e.g. [67]). As mentioned above, anisotropy in the shape of the interacting tensile microcracks is likely to exert significant influence on the orientation of the final through-going shear fracture. Further work is underway to model the interactions of cracks of general ellipsoidal ($a>b>c$) shape, as opposed to the spheroidal ($a=b\gg c$) shapes used in this study. The expressions for the elastic field of a general ellipsoid are only approximate and depend on elliptic integrals

[55,56,59,60,52]. However, we believe that the initial results from this study (see also [68]) with 'penny-shaped' (spheroidal) cracks and an isotropic matrix are fundamental and robust: the interaction, and eventual coalescence, of tensile microcracks is a 3-D process leading to brittle shear failure planes oriented obliquely to all three principal stresses.

The key results of this numerical study into shear fracture development in 3-D suggest that further experimental work is required. More systematic polyaxial (truly triaxial) laboratory experiments, with failure dynamically controlled by the rate of acoustic emissions [23], are needed to map out shear fracture nucleation and propagation in 3-D and 4-D. In particular, we would like to see more published measurements from polyaxial experiments of the actual orientation of failure planes with respect to the principal stress axes (c.f. [16]).

7. Summary

The 3-D micromechanical models of crack interactions presented in this paper are an attempt to improve on current theories of shear failure that cannot explain the formation of contemporaneous polymodal fractures orientated oblique to all three principal stress axes. Failure criteria that are limited to predict only conjugate bimodal faults are two-dimensional approximations of geological reality. Numerical modelling of the elastic field in 3-D around isolated and *en echelon* arrays of tensile cracks uses the classical formulation of Eshelby [55,56], based on the closed form expressions by Ju and Sun [52]. Tensile microcracks are modelled as finite 3-D ellipsoidal voids in a linear isotropic elastic matrix, and subjected to small opening strains. The 2-D views of the complete 3-D elastic field match results from previous work based on 2-D thin sheet or plane strain simplifications (e.g. [32]). Lobes of high tensile stress are formed at the ends of a tensile crack, and displaced to either side. The loci of maximum tensile stress are mapped in two orthogonal planes, and for a penny-shaped crack, the loci are identical, forming an indented toroidal pattern in 3-D. Tensile stress interactions between neighbouring cracks are most likely along these loci [26], leading to *en echelon* arrays of interacting cracks. The model predicts that a 3-D population of tensile mode I microcracks, each aligned parallel to the σ_1–σ_2 principal plane of the remote stress field, will interact to form a shear fracture nucleus that is oblique to the microcracks and oblique to all three principal stresses. Existing experimental data confirm that once formed in a certain orientation, a composite shear fracture propagates broadly within its own plane, through the coalescence of many tensile microcracks. Our fundamental results can successfully explain the orientation of newly-formed quadrimodal shear fractures such as the deformation bands observed at Gruinard Bay, Scotland and in many other natural examples. We speculate that published field data of apparently 'conjugate' bimodal faults with a finite spread of poles in the stereonets is a further manifestation of this oblique shear fracture phenomenon (see for example [69], their Fig. 2). The spread in orientations is often ascribed to 'noise', due to some combination of measurement error, anisotropy, heterogeneous remote stress fields etc. Similarly, results from many polyaxial rock deformation experiments describe the final shear plane as 'sub-parallel' to σ_2. We believe that these variations in the orientation of the shear plane may be of primary significance (i.e. not just 'noise'), and at least partially reflect the oblique nucleation of many brittle shear fractures under triaxially compressive conditions in the lithosphere.

Acknowledgements

Many thanks to Lizhi Sun for the help in benchmarking the external field solution of Eshelby, and to Phil Meredith and Martin Casey for the insightful discussions at DRT in Zürich (May 2005). We thank Nicola De Paola and an anonymous reviewer for the critical comments which improved the manuscript. The GMT mapping software of [70] was used to create the location maps in Fig. 3.

Appendix A

The corrected expressions given below are based on those provided by [52], and have been used to benchmark the numerical code used in this study by reproducing the published solutions of external fields in [59] and [58].

The signs in the first terms of the first two components of the exterior-point Eshelby tensor need to be reversed; so that Eq. (A.1) in [52] should read

$$S_{11}^{(1)}(\lambda) = \left[4v_0\frac{2}{\alpha^2-1}\right]g(\lambda) - \frac{2}{3(\alpha^2-1)}\rho_1^3(\lambda) + \left[4v_0\frac{2}{\alpha^2-1}\right]\rho_1(\gamma)\rho_2^2(\lambda)$$

and similarly, Eq. (A.2) in [52] should read

$$S_{12}^{(1)}(\lambda) = S_{13}^{(1)}(\lambda) = \left[4v_0 + \frac{2\alpha^2-1}{\alpha^2-1}\right]g(\lambda) + \left[4v_0 - \frac{2\alpha^2}{\alpha^2-1}\right]\rho_1(\lambda)\rho_2^2(\lambda)$$

References

[1] C.A. Coulomb, Sur une application des règles de Maximis et Minimis a quelques problèmes de statique relatifs à l'Architecture, Acad. Roy des Sciences de math et de physique par divers savans, vol. 7, 1773, pp. 343–382.

[2] Z. Reches, Analysis of faulting in three-dimensional strain field, Tectonophysics 47 (1978) 109–129.

[3] Z. Reches, Faulting of rocks in three-dimensional strain fields II. Theoretical analysis, Tectonophysics 95 (1983) 133–156.

[4] A. Aydin, Z. Reches, Number and orientation of fault sets in the field and in experiments, Geology 10 (1982) 107–112.

[5] R.W. Krantz, Multiple fault sets and 3-dimensional strain—theory and application, J. Struct. Geol. 10 (1988) 225–237.

[6] R.W. Krantz, Orthorhombic fault patterns — the odd axis model and slip vector orientations, Tectonics 8 (1989) 483–495.

[7] E.M. Anderson, The Dynamics of Faulting and Dyke Formation with Applications to Britain, Oliver and Boyd, Edinburgh, 1951.

[8] J. Jaeger, N.G.W. Cook, Fundamental of Rock Mechanics, 3rd edition, Chapman & Hall, London, 1979, p. 593.

[9] J.F. Dewey, R.E. Holdsworth, R.A. Strachan, Transpression and transtension zones, in: R.E. Holdsworth, R.A. Strachan, J.F. Dewey (Eds.), Continental Transpressional and Transtensional Tectonics, Geological Society Special Publications, vol. 135, 1998, pp. 1–14.

[10] R.R. Jones, R.E. Holdsworth, K.J.W. McCaffrey, P. Clegg, E. Tavarnelli, Scale dependence, strain compatibility and heterogeneity of three-dimensional deformation during mountain building: a discussion, J. Struct. Geol. (27) (2005), doi:10.1016/j.jsg.2005.04.001.

[11] R.H. Sibson, Fluid involvement in normal faulting, J. Geodyn. 29 (2000) 469–499.

[12] K.R. Sternlof, J.R. Chapin, D.D. Pollard, L.J. Durlofsky, Permeability effects of deformation band arrays in sandstone, AAPG Bull. 88 (2004) 1315–1329.

[13] J. Byerlee, Friction of rock, Pure Appl. Geophys. 116 (1978) 615–626.

[14] K. Mogi, Effect of the intermediate principal stress on rock failure, J. Geophys. Res. 72 (1967) 5117–5131.

[15] G. Oertel, The mechanism of faulting in clay experiments, Tectonophysics 2 (1965) 343–393.

[16] Z. Reches, J. Dieterich, Faulting of rocks in three-dimensional strain fields I. Failure of rocks in polyaxial, servo-control experiments, Tectonophysics 95 (1983) 111–132.

[17] L.B. Colmenares, M.D. Zoback, A statistical evaluation of intact rock failure criteria constrained by polyaxial test data for five different rocks, Int. J. Rock Mech. Min. Sci. 39 (2002) 695–729.

[18] M.S. Paterson, Experimental Rock Deformation — the Brittle Field, Springer-Verlag, Berlin, 1978, p. 254.

[19] D.E. Moore, D.A. Lockner, The role of microcracking in shear-fracture propagation in granite, J. Struct. Geol. 17 (1995) 95–114.

[20] C. Chang, B. Haimson, True triaxial strength and deformability of the German Continental Deep Drilling Program (KTB) deep hole amphibolite, J. Geophys. Res. 105 (2000) 18,999–19,013.

[21] S. Peng, A.M. Johnson, Crack growth and faulting in cylindrical specimens of Chelmsford granite, Int. J. Rock Mech. Min. Sci. 9 (1972) 37–86.

[22] T.-F. Wong, Micromechanics of faulting in Westerly granite, Int. J. Rock Mech. Min. Sci. Geomech. Abstr. 19 (1982) 49–64.

[23] D.A. Lockner, J.D. Byerlee, V. Kuksenko, A. Ponomarev, A. Sidorin, Quasi-static fault growth and shear fracture energy in granite, Nature 350 (1991) 39–42.

[24] D.A. Lockner, J.D. Byerlee, V. Kuksenko, A. Ponomarev, A. Sidorin, Observations of quasistatic fault growth from acoustic emissions, in: B. Evans, T. Wong (Eds.), Fault Mechanics and Transport Properties of Rocks, Academic Press, London, 1992.

[25] P.W.J. Glover, J.B. Gomez, P.G. Meredith, Fracturing in saturated rocks undergoing triaxial deformation using complex electrical conductivity measurements: experimental study, Earth Planet. Sci. Lett. 5621 (2000) 201–213.

[26] Z. Reches, D.A. Lockner, Nucleation and growth of faults in brittle rocks, J. Geophys. Res. 99 (1994) 18159–18173.

[27] A.A. Griffith, The phenomena of rupture and flow in solids, Trans. R. Soc. A221 (1920) 163–179.

[28] R.A. Sack, Extension of Griffith's theory of rupture to three dimensions, Proc. R. Soc. 58 (1946) 729–736.

[29] W.F. Brace, An extension of the Griffith theory of fracture to rocks, J. Geophys. Res. 65 (1960) 3477–3480.

[30] W.F. Brace, E.G. Bombolakis, A note on brittle crack growth in compression, J. Geophys. Res. 68 (1963) 3709–3713.

[31] H. Horii, S. Nemat-Nasser, Brittle failure in compression: splitting, faulting and brittle–ductile transition, Philos. Trans. R. Soc. Lond. A319 (1986) 337–374.

[32] D.D. Pollard, P. Segall, Theoretical displacements and stresses near fractures in rock: with applications to faults, joints, veins, dikes, and solution surfaces, in: B.K. Atkinson (Ed.), Fracture Mechanics of Rock, Academic Press, London, 1987.

[33] C.G. Sammis, M.F. Ashby, The failure of brittle porous solids under compressive stress states, Acta Metall. 34 (1986) 511–526.

[34] G.C.P. King, C.G. Sammis, The mechanisms of finite brittle strain, Pure Appl. Geophys. 138 (1992) 611–640.

[35] N.C. Davatzes, A. Aydin, P. Eichhubl, Overprinting faulting mechanisms during the development of multiple fault sets in sandstone, Chimney Rock fault array, Utah, USA, Tectonophysics 363 (2003) 1–18.

[36] A.G. Koestler, W.U. Ehrmann, Description of brittle extensional features in chalk on the crest of a salt ridge (NW Germany), in: A. M. Roberts, G. Yielding, B. Freeman (Eds.), The Geometry of Normal Faults, Geological Society, London, Special Publication, vol. 56, 1991, pp. 113–123.

[37] R.R. Jones, P.W.G. Tanner, Strain partitioning in transpression zones, J. Struct. Geol. 17 (1995) 793–802.

[38] R.R. Jones, R.E. Holdsworth, W. Bailey, Lateral extrusion in transpression zones: the importance of boundary conditions, J. Struct. Geol. 19 (1997) 1201–1217.

[39] J.G. Crider, Oblique slip and the geometry of normal-fault linkage: mechanics and a case study from the Basin and Range in Oregon, J. Struct. Geol. 23 (2001) 1997–2009.

[40] J. Imber, R.E. Holdsworth, K.J.W. McCaffrey, R.W. Wilson, R.R. Jones, R.W. England, G. Gjeldvik, Early Tertiary sinistral transpression and fault reactivation in the western Vøring Basin, Norwegian Sea: implications for hydrocarbon exploration and pre-break up deformation in ocean margin basins, AAPG Bull. 89 (2005) 1043–1069.

[41] N. De Paola, R.E. Holdsworth, K.J.W. McCaffrey, The influence of lithology and pre-existing structures on reservoir-scale faulting patterns in transtensional rift zones, J. Geol. Soc. (Lond.) 162 (2005) 471–480.

[42] G.J. Potts, S.M. Reddy, Construction and systematic assessment of relative deformation histories, J. Struct. Geol. 21 (1999) 1245–1253.

[43] G.J. Potts, S.M. Reddy, Application of younging tables to the construction of relative deformation histories — 1: fracture systems, J. Struct. Geol. 22 (2000) 1473–1490.

[44] A. Aydin, Small faults formed as deformation bands in sandstone, Pure Appl. Geophys. 116 (1978) 913–930.
[45] N.H. Woodcock, J.R. Underhill, Emplacement-related fault patterns around the Northern Granite, Arran, Scotland, Bull. Geol. Soc. Am. 98 (1987) 515–527.
[46] K. Mair, I. Main, S. Elphick, Sequential growth of deformation bands in the laboratory, J. Struct. Geol. 22 (2000) 25–42.
[47] Y. Du, A. Aydin, Interaction of multiple cracks and formation of echelon crack arrays, Int. J. Numer. Anal. Methods Geomech. 15 (1991) 205–218.
[48] D.A. Lockner, T.R. Madden, A multiple-crack model of brittle fracture (1) Non-time dependent simulations, J. Geophys. Res. 96 (1991a) 19623–19642.
[49] D.A. Lockner, T.R. Madden, A multiple-crack model of brittle fracture (2) Time dependent simulations, J. Geophys. Res. 96 (1991b) 19643–19654.
[50] D.D. Pollard, P. Segall, P.T. Delaney, Formation and interpretation of dilatant echelon cracks, Bull. Geol. Soc. Am. 93 (1982) 1291–1303.
[51] J.G. Crider, D.D. Pollard, Fault linkage: three-dimensional mechanical interaction between echelon normal faults, J. Geophys. Res. 103 (1998) 24,373–24,391.
[52] J.W. Ju, L.Z. Sun, Effective elastoplastic behaviour of metal matrix composites containing randomly located aligned spheroidal inhomogeneities. Part 1: micromechanics based formulation, Int. J. Solids Struct. 38 (2001) 183–201.
[53] M. Kachanov, On the problems of crack interactions and crack coalescence, Int. J. Fract. 120 (2003) 537–543.
[54] H.M. Shodja, I.Z. Rad, R. Soheilifard, Interacting cracks and ellipsoidal inhomogeneities by the equivalent inclusion method, J. Mech. Phys. Solids 51 (2003) 945–960.
[55] J.D. Eshelby, The determination of the elastic field of an ellipsoidal inclusion, and related problems, Proc. R. Soc. Lond. A241 (1957) 376–396.
[56] J.D. Eshelby, The elastic field outside an ellipsoidal inclusion, Proc. R. Soc. Lond. A252 (1959) 561–569.
[57] S.A.F. Murrell, P.J. Digby, The theory of brittle fracture initiation under triaxial stress conditions — I, Geophys. J. R. Astron. Soc. 19 (1970) 309–334.
[58] M.A. Sadowsky, E. Sternberg, Stress concentration around a triaxial ellipsoidal cavity, Trans. ASME 71 (1949) A149–A157.
[59] T. Mura, Micromechanics of Defects in Solids, 2nd Edition, Kluwer, Dordrecht, The Netherlands, 1987, p. 587.
[60] J.W. Ju, L.Z. Sun, A novel formulation for the exterior-point Eshelby's tensor of an ellipsoidal inclusion, J. Appl. Mech. 66 (1999) 570–574.
[61] F. Chalon, F. Montheillet, The interaction of two spherical gas bubbles in an infinite elastic solid, J. Appl. Mech. 70 (2003) 789–798.
[62] M.K. Kassir, G.C. Sih, Three-dimensional stress distribution around an elliptical crack under arbitrary loadings, J. Appl. Mech. 33 (1966) 601–611.
[63] J.-P. Petit, M. Barquins, Can natural faults propagate under mode II conditions? Tectonics 7 (1988) 1243–1256.
[64] S.J.D. Cox, C.H. Scholz, On the formation and growth of faults: an experimental study, J. Struct. Geol. 10 (1988a) 413–430.
[65] S.J.D. Cox, C.H. Scholz, Rupture initiation in shear fracture of rocks: an experimental study, J. Geophys. Res. 93 (1988b) 3307–3320.
[66] S. Crampin, J.H. Lovell, A decade of shear-wave splitting in the earths crust — what does it mean — what use can we make of it — and what should we do next, Geophys. J. Int. 107 (1991) 387–407.
[67] L. Louis, C. David, P. Robion, Comparison of the anisotropic behaviour of undeformed sandstones under dry and saturated conditions, Tectonophysics 370 (2003) 193–212.
[68] D. Healy, R.R. Jones, R.E. Holdsworth, Three-dimensional brittle shear fracturing by tensile crack interaction, Nature 439 (2006) 64–67.
[69] D.C.P. Peacock, D.J. Sanderson, Effects of layering and anisotropy on fault geometry, J. Geol. Soc. (Lond.) 149 (1992) 793–802.
[70] P. Wessel, W.H.F. Smith, New, improved version of the Generic Mapping Tools released, EOS Trans. AGU 79 (1998) 579.